



RESEARCH ARTICLE | SEPTEMBER 11 2024

Ti-Zr-Nb-(V) refractory alloy coatings deposited by high-power impulse magnetron sputtering: Structure, mechanical properties, oxidation resistance, and thermal stability

A. Fraile ; D. Cavaleiro ; A. Bondarev ; S. C. Middleburgh ; W. E. Lee ; F. Fernandes



J. Vac. Sci. Technol. A 42, 063101 (2024)

<https://doi.org/10.1116/6.0003864>



Articles You May Be Interested In

Superconductivity in TiZrNb and TiZrNbHf bulk equimolar alloys


Low Temp. Phys. (August 2024)

Laser direct forming submicron Cu-rich particle structural TiZrNbCu_x medium-entropy alloy coatings to achieve desirable anti-bacterial property

J. Laser Appl. (March 2024)

Medium-entropy Ti-Zr-Nb thin films prepared by magnetron sputtering: Structural TEM study

AIP Conf. Proc. (October 2024)

 **Advance your science and your career as a member of AVS**

[LEARN MORE](#)

Ti-Zr-Nb-(V) refractory alloy coatings deposited by high-power impulse magnetron sputtering: Structure, mechanical properties, oxidation resistance, and thermal stability

Cite as: J. Vac. Sci. Technol. A 42, 063101 (2024); doi: 10.1116/6.0003864

Submitted: 26 June 2024 · Accepted: 22 August 2024 ·

Published Online: 11 September 2024



View Online



Export Citation



CrossMark

A. Fraile,^{1,a)} D. Cavaleiro,² A. Bondarev,^{3,b)} S. C. Middleburgh,¹ W. E. Lee,¹ and F. Fernandes^{2,4,c)}

AFFILIATIONS

¹Nuclear Futures Institute, Bangor University, Bangor LL57 1UT, United Kingdom

²Department of Mechanical Engineering, CEMMPRE, ARISE, University of Coimbra, Rua Luís Reis Santos, Coimbra 3030-788, Portugal

³Bernal Institute, School of Engineering, University of Limerick, Limerick V94 T9PX, Ireland

⁴CIDEM, ISEP Polytechnic of Porto, Rua Dr. António Bernardino de Almeida, Porto 4249-015, Portugal

^{a)}Author to whom correspondence should be addressed: albertofrailegarcia@gmail.com

^{b)}Electronic mail: andrey.bondarev@ul.ie

^{c)}Electronic mail: fid@isep.ipp.pt

ABSTRACT

A series of TiZrNb(V) high entropy alloy-based metallic coatings have been deposited using high-power impulse magnetron sputtering (HiPIMS), with variable V concentrations and constant ratios among the other metals. The coatings were analyzed regarding their composition, surface and cross-sectional morphologies, microstructure, roughness, mechanical properties, oxidation resistance, and thermal stability. The structure of the deposited coatings reveals a transition from the bcc crystal structure to an amorphous phase as the V concentration increases. The addition of V also led to a decrease in roughness Ra and an improvement in adhesion, while it did not affect hardness, which remained at ~10–11 GPa for all samples. Annealing under a protective atmosphere at 400 °C caused structural ordering, which was followed by an increase in mechanical properties. The purpose of the present paper is, therefore, to present a study on the deposition of TiZrNb coatings with increasing V concentration prepared by HiPIMS and to understand the role of V concentration on their structure, chemical composition, mechanical properties, and oxidation resistance. Comparison of the results with those achieved for a reference TiZrNb coating is presented too.

© 2024 Author(s). All article content, except where otherwise noted, is licensed under a Creative Commons Attribution (CC BY) license (<https://creativecommons.org/licenses/by/4.0/>). <https://doi.org/10.1116/6.0003864>

I. INTRODUCTION

Nuclear energy, both fission and future fusion, in alliance with renewables, has a most important role to play toward the planet's net zero CO₂ goals. It is a perfect example where state of the art materials' science is needed to design, develop, and test new materials for extreme environments. The challenging environments associated with next-generation fission^{1–3} and fusion^{4–9} are likely to vary markedly according to the reactor design and the component of interest, but may involve extremes of temperature, radiation

damage, corrosion, stress, and heat flux. Further, such conditions are also faced in other advanced engineering applications.^{10,11}

On the road to improve the mechanical properties of a material, there are many milestones considering the reconfiguration of the microstructure with various design strategies, from multilayered materials^{12–14} to all kinds of nanocrystalline structures.^{15,16} Today, the expanded compositional freedom afforded by high entropy alloys (HEAs) and other high entropy materials represents a unique opportunity for the design of alloys for harsh

environments,^{17–20} such as advanced nuclear applications,^{21–23} or other applications where current engineering alloys fall short. Surface coating technology has brought new vitality to the development of HEAs,^{24–27} which relieves the restrictions of preparation and industrial application caused by the cost of bulk HEAs and enhances the possibility of rapid design for new materials. Many publications have reported that HEA coatings demonstrate excellent corrosion resistance in aggressive environments.²⁸ In general, the factors affecting the corrosion resistance of HEA coatings include the formation of a passive layer, coatings composition, and microstructure of the coating surface, which are closely associated with the composition design and preparation process parameters.

In this work, a series of TiZrNb(V) medium entropy alloy (MEA)-based metallic coatings have been developed. The choice is based on the previous work in this system in bulk form. The NbTiVZr_x (x = 0.5, 1, and 2) MEAs were experimentally confirmed to be a single-phase MEA system.²² Further, homogenization at 1200 °C for 100h resulted in single-phase bcc microstructures without compositional microsegregation observed in as-cast or slow cooled samples.²² Also important, the system has been recently scrutinized in terms of radiation resistance properties. Kadyrzhanov *et al.*²⁹ studied the kinetics of accumulation of radiation damage in the near-surface layer of NbTiVZr alloys upon irradiation with Kr¹⁵⁺ ions and fluences of 10¹⁰–10¹⁵ ion/cm². Further, the role played by V in HEAs has been explored using density functional theory (DFT) calculations by Lin-Vines *et al.*³⁰ The preferential formation of V split interstitials over any of the other elements provides a mechanism for the observed strengthening in the material. Further, V appears unique among other elements for providing high strengthening in both the fcc Co-Cr-Fe-Mn-Ni-V and bcc Cr-Mo-Nb-Ta-V-W-Hf-Ti-Zr HEA families.³¹

The mechanical properties of coatings depend on the deposition technique employed. Over the past decade, important advancements in magnetron sputtering deposition technologies have emerged, to produce highly ionized fluxes of sputtered material. These innovations have provided greater control over the energetic ion bombardment, including the energy and direction of the deposited species. Among the remarkable developments are two techniques: high-power impulse magnetron sputtering (HiPIMS), also known as high-power pulsed magnetron sputtering, and modulated pulsed power magnetron sputtering (MPPMS). Both HiPIMS and MPPMS involve applying exceptionally high target power densities to achieve enhanced plasma densities and subsequent ionization of the sputtered material. Researchers have already investigated the impact of the different deposition parameters on the properties of coatings. More compact coatings with improved mechanical, physical, tribological, adhesion to the substrate, and thermal properties have been reported by using these new technologies.^{32,33} Since, for the desired application, an alloy with the best possible properties is required and for that a formidable structure and adhesion is crucial, HiPIMS will be the deposition method used in this work; in addition to the fact that Hajihoseini and Gudmundsson³⁴ obtained superior results for V-based coatings using this deposition method.

When dealing with coatings, one must consider adhesion and tribological properties and not only those properties encountered

in the bulk material. TiZr alloys are a material well studied by a large number of authors that prove their excellent tribological properties and resistance to oxidation.^{35,36} According to Ji *et al.*,³⁷ the addition of Nb has a very positive impact on the oxidation resistance of these alloys, mainly in terms of pitting. Therefore, in theory, the TiZrNb alloy is a good base for a high-performance HEA for very harsh environments. TiZrNb alloys have great applicability, mainly for biomedical applications, namely, for prostheses with better tribological properties and oxidation resistance, when compared to the Ti6Al4V alloy (very common in this type of application). Hu *et al.*³⁸ suggest the use of this alloy in a massive way, completely replacing the Ti6Al4V alloy. After several cold calendaring processes and subsequent annealing, the values of fracture toughness and Young's modulus were achieved for the TiZrNb alloy in relation to the Ti6Al4V alloy. Mu *et al.*³⁹ suggest the use of the TiZrNb alloy as a coating to apply on the Ti6Al4V alloy (solid material) in order to improve its resistance to wear and oxidation. Forty and Karditsas⁴⁰ confirmed that Zr alloys should be considered for fission applications and especially when long longevity is desired, which meets the application needs of this work. Additionally, the addition of V to HEA can be advantageous for several reasons. As this is a refractory metal, a very positive impact on thermal stability is expected, as well as on wear resistance at high temperatures, as is the case with the CrFeHfMnTiTaV alloy.⁴¹ According to Yin *et al.*,³¹ V distorts the crystal lattice of the bcc structure, a structure that is quite dominant for alloys with Ti and Zr. In the bulk form, Wang *et al.*⁴² showed that the presence of V in solid solution favors a grain size refinement. Thus, the effect of V addition must be studied for other systems. Previous experimental and modeling studies of the Zr-V system assessed materials produced by magnetron sputtering that highlighted the preference for amorphous structures to preferentially form over crystalline structures in specific ranges of the binary system.^{43,44}

Also important, recent studies used HiPIMS to produce Ti-based alloy coatings. To mention just a few examples, Marczewski *et al.* compared the microstructure and mechanical properties of Ti-Nb alloys as created by conventional powder metallurgy, mechanical alloying, and HiPIMS.⁴⁵ Lou *et al.* employed HiPIMS for the fabrication of (TiZrNbSiMo)_{1-x}N_x HEAs coatings paying attention to the effects of nitrogen addition.⁴⁶ Kamrudin Bachani *et al.* studied TiZrNbTaFeN HEA coatings prepared by HiPIMS. The effect of nitrogen flow rate on the microstructure, mechanical and tribological performance, electrical properties, and corrosion characteristics was reported.⁴⁷ These studies highlighted the potential of using HiPIMS to develop protective coatings.

The purpose of the present paper is, therefore, to present a study on the deposition of TiZrNb coatings with increasing V concentration prepared by HiPIMS and to understand the role of V concentration on their structure, chemical composition, mechanical properties, and oxidation resistance. Comparison of the results with those achieved for a reference TiZrNb coating is presented too.

II. EXPERIMENT

A. Deposition process

TiZrNbV coatings with different V concentrations, ranging from 0 to 27.89 at. %, were deposited in a Hartec chamber using an

HiPIMS power supply (HiPIMS Cyprium™ III plasma generator, Zpulsor Inc.) working in deep oscillation magnetron sputtering (DOMS) mode. The targets were acquired from Photon Export (<https://photonexport.com/>). One high purity (99.9%) TiZr compound target (47 at. % Ti–53 at. % Zr) with dimensions of $150 \times 150 \times 8 \text{ mm}^3$, containing 20 holes of 10 mm diameter evenly distributed along the preferential erosion zone of the race track, was used for the deposition of the coatings. This target architecture allows the tuning of the chemical composition of the films by filling/changing the holes with pellets of different elements (Nb and V). Five holes were filled with Nb (99.9%) cylindrical rods and the remaining holes with incremental number of V (99.9%) cylindrical rods, to achieve a progressive increase of V content on the TiZrNbV films.

The coatings were deposited onto silicon wafers (111) for chemical, cross-sectional, and surface morphology analysis; structural analysis; and mechanical properties evaluation (hardness and Young's modulus). Al_2O_3 substrates ($10 \times 0.8 \text{ mm}^2$) were used for oxidation resistant tests. For adhesion evaluation through scratch testing, M2 steel disks ($\text{Ø}24 \times 8 \text{ mm}^2$) were used as substrates.

Before the deposition, all the substrates were ultrasonically cleaned in acetone and alcohol for 15 min each and then mounted on a rotating substrate holder that revolved at around 23 rpm in the center axis of the chamber. Prior to the deposition, the chamber was evacuated down to a pressure of $1 \times 10^{-4} \text{ Pa}$. The TiZr target was then cleaned in Ar (discharge pressure—0.5 Pa) for 10 min by applying an average peak power (Pa) of 1200 W, a charging voltage (DC_{int}) of 350 V, and a pulse duration (D) of $1500 \mu\text{s}$, while having the shutter in front to avoid cross contamination between the target and the substrate. After, substrate etching with Ar ions using a DC-pulsed power supply was conducted at a pressure of 0.5 Pa applying a bias of 320 V for 50 min. After the etching, all the depositions were conducted at a working pressure of 0.5 Pa. The following parameters were kept constant during the depositions: average peak power at the target of 1200 W, charging voltage of 350 V established at the capacitors, constant on time (ton) of $6 \mu\text{s}$, an oscillation period (T) of $70 \mu\text{s}$, and a pulse duration of $1500 \mu\text{s}$. To keep these parameters constant, the pulse frequency (F) was automatically adjusted by the DOMS power supply software. In all the cases, the deposition time was set to achieve a thickness of the coatings close to $2 \mu\text{m}$. The denomination adopted for the coatings, as well as the summary of the deposition conditions, are shown in Table I.

B. X-ray diffraction and nanohardness

The crystallographic structure of the coatings was investigated with x-ray diffraction (XRD) using a copper $\text{K}\alpha_1$ radiation ($\lambda = 1.54 \text{ \AA}$) using GIXRD geometry with a parallel beam in θ - 2θ mode (2θ range: 5° – 110° , anode current: 40 A and voltage 45 V, incidence angle $\omega = 1^\circ$). The XRD equipment employed was an X'Pert Pro x-ray diffractometer from Philips.

The hardness and Young's modulus of the coatings were evaluated by nanoindentation. The nanoindenter equipment was a NanoTester Platform 1 from MicroMaterials.

This test was conducted using a Berkovich diamond indenter. The indentation depth was kept less than 10% of the coating thickness to avoid the contribution of the substrate. The nanoindentation tests were carried out 12 times in every specimen to obtain reliable statistics.

C. Scanning electron microscopy and wavelength-dispersive x-ray spectroscopy

The cross-sectional and surface morphology of the coatings were studied using a Zeiss Merlin scanning electron microscope (SEM) equipped with wavelength-dispersive spectroscopy (WDS) system for chemical composition analysis. Standard specimens were used for calibration.

D. Atomic force microscopy (AFM)

The surfaces were examined using AFM. The employed AFM was a Veeco Dimension 3100 AFM with a Veeco NanoScope V controller. We used it in tapping mode using a PPP-NCHR probe manufactured by Nanosensors.

E. Adhesion tests

The adhesion of the coatings to the substrates was evaluated using a scratch tester (Scratch test control Revetest Csem). The following parameters were used during the tests: linearly increasing load from 2 to 100 N, with a feed speed of 10 mm/min and a load increment of 100 N/min. In this test, a Rockwell C spherical indenter with a radius of 0.2 mm was employed. Subsequently, the results were evaluated using an optical microscope with a magnification of $200\times$.

TABLE I. HiPIMS deposition parameters used to fabricate multicomponent TiZrNb(V) coatings, V_p is the peak voltage, I_p is the peak current, P_p is the peak power, and F_i is the frequency, which is automatically adjusted to maintain the average power applied to the target.

Coating designation	Number of Nb pellets	Number of V pellets	Deposition time (min)	HiPIMS parameters			
				V_p (V)	I_p (A)	P_p (kW)	F_i (Hz)
V_0	5	0	65	1210	96	116	156
V_1	5	5	60	1220	82	100	157
V_2	5	10	55	1236	64	79	156
V_3	5	15	50	1237	49	61	156

20 January 2025 18:57:12

F. Oxidation resistance tests

The oxidation resistance of the coatings was evaluated in two different ways: using dynamic tests and isothermal tests. For both, thermogravimetry analysis (TGA) equipment was used, maintaining an oxygen atmosphere with a purity of 99.9% and the mass gain due to oxidation was continuously measured using a microbalance, with a precision of 0.01 mg, at time intervals of 2 s.

Dynamic oxidation tests were carried out in order to determine the temperature at which the coatings begin the oxidation process. The coatings were, thus, heated from room temperature to 1200 °C, at a rate of 20 °C/min, and the mass gain was recorded. Isothermal oxidation tests were performed by subjecting the coated samples to an isothermal temperature of 400 °C for 1h. This temperature was selected through the analysis of dynamic tests. The heating rate used to reach the isothermal temperature was 20 °C/min. At the end, the cross-sectional morphology and respective elemental maps distribution were reassessed using SEM-EDS.

III. RESULTS AND DISCUSSION

A. Chemical analysis and x-ray diffraction

Figure 1 displays the chemical compositions of the coatings acquired through WDS. As anticipated, the stepwise incorporation of V pellets into the target resulted in coatings with progressively higher V concentrations. Notably, the ratios of Zr/Ti, Nb/Ti, and Nb/Zr, as evident in Fig. 1 (inset), remained constant. Thus, the addition of vanadium does not alter the proportion between these elements. Consequently, it can be inferred that variations in coating properties are attributable solely to the fluctuation in vanadium content and deposition conditions, without affecting the proportion between the remaining elements. Going forward, the coatings will be designated as V₀, V₁, V₂, and V₃. Here, V₀ represents the TiZrNb ternary coating, while the indices 1, 2, and 3 indicate an increasing concentration of V in the TiZrNbV coatings. It is important to note that oxygen was present in all coatings at a level of

approximately 7%–10%. We believe this high concentration can be attributed not only to residual oxygen from the deposition process but also to the fact that the analysis was conducted on the surface after exposure to ambient air.

The x-ray diffraction patterns of the various samples are depicted in Fig. 2. The XRD patterns of the coatings are presented in the range of 38°–50° 2θ, as this range captures the sole diffraction peak identified during wide-range scanning. Notably, V₀ and V₁ coatings exhibit a high-intensity diffraction peak situated at approximately ~43° 2θ. This specific peak falls between the (110) peaks of Zr (at 41.8°) and Ti (at 45°), suggesting the formation of a substitutional solid solution. The structures of these coatings align with a body-centered cubic (bcc) structure, where different elements randomly occupy substitutional positions within the bcc framework.⁴⁸ All the samples had similar dimensions and revealed comparable thicknesses (approximately 2 μm); thus, the conspicuous intensity observed in the V₀ and V₁ coatings cannot be ascribed solely to a mere increase in the quantity of diffracting material. The noteworthy intensity of the diffraction peak, especially in the case of the V₀ coating, implies a preferred orientation (110). This indicates that the crystallographic planes (110) are aligned parallel to the sample surface in the V₀ coating.

One conceivable reason behind the anomalous intensity of the (110) diffraction peak could be the development of a mosaic structure, wherein diffraction domains exhibit only slight misorientation with respect to one another and the underlying substrate. As the diffraction patterns were acquired using an x-ray parallel beam, in contrast to conventional Bragg–Brentano mode, the range of tilts for the diffracting domains relative to the film surface is significantly smaller. Consequently, this often leads to reduced diffraction intensity. However, in cases where the diffraction domains are marginally misaligned in relation to each other and the film surface, the number of domains increases substantially, giving rise to a much higher intensity of the XRD peaks. A similar observation was observed for TiSiN films deposited by the same technology.⁴⁸

20 January 2025 18:57:12

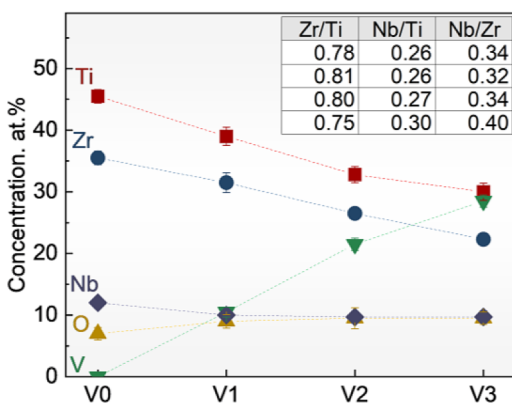


FIG. 1. Chemical composition of the coatings in at. %. Note that in some cases the error bar is smaller than the symbol. The inset in the top right corner presents the Zr/Ti, Nb/Ti, and Nb/Zr ratios of the four samples, starting from V₀ and ending in V₃.

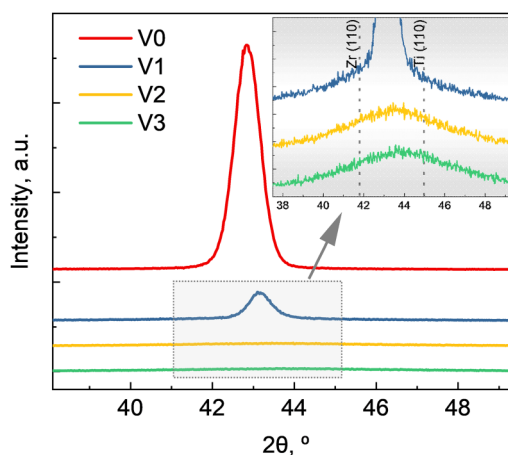


FIG. 2. GIXRD diffraction patterns of the TiZrNb(V) coatings.

The intensity of the diffraction peak in sample V_0 is five times greater than that in sample V_1 , indicating a reduction in crystallinity with the introduction of V into the coating. Additionally, the introduction of V to the V_1 coating shifts the diffraction peak to higher angles, implying a decrease in the lattice parameter.⁴⁹ It is worth noting that the atomic radius of V is 135 pm, whereas the atomic radii of Zr and Nb are 155 and 145 pm, respectively.⁵⁰ As a result, the substitution of some Zr and Nb atoms by V leads to a shift of the diffraction peaks to larger angles, attributed to the smaller atomic radius of V. XRD peak positions vs V concentration will discuss and illustrate in Sec. III F.

Further increase in V content in the coatings leads to the formation of x-ray amorphous structure, as indicated by the broad, low-intensity peaks (Fig. 2, inset). The probability of forming an amorphous structure in the alloy increases when the number of components in the HEAs system is greater than the ternary.⁵¹ In addition, the increasing V content stabilized the amorphous phase and reduced the driving force to form a crystalline structure leading to formation of dense amorphous structure like it was found for other HEA obtained by PVD methods.⁵²

It is worth mentioning that DFT calculations and experiments confirmed that an amorphous VZr solid solution is more stable than a random body-centered solid solution of the two elements.⁴⁸ Additionally, crystallization of the V_2Zr Laves phase in VZr alloys is predicted to occur at relatively high temperatures.⁴⁸

B. Morphology of the coatings

The evolution of cross-sectional and surface morphology of the coatings with V additions is depicted in Fig. 3. Figure 3(a) reveals that the cross-sectional morphology of sample V_0 is columnar. In Fig. 3(b), the sample V_1 exhibits a similar morphology but more compact. For sample V_2 , Fig. 3(c) shows a significantly more compact cross section with only a few traces of columnar attributes. Finally, in sample V_3 , the coating is fully compacted, as illustrated in Fig. 3(d). It can be concluded that the addition of V has a notably positive effect on increasing the compactness level of the samples. This enhancement could be crucial in improving properties such as hardness and corrosion resistance. It should be noted here that the increasing V concentration gradually decrease the Pp (peak power) value. The decrease of Pp value is normally associated with the generation of less compact and consequently more open morphologies. In fact, a decrease of Pp is associated with the reduction in the ionization fraction of the metallic elements and the corresponding decrease in their energy.^{48,53} In the present work, the decrease in Pp leads to more compact morphologies. Indeed, it is established in the literature that amorphous coatings typically possess a compact structure.^{48,54}

Concerning surface morphology, the V_0 sample, as shown in Fig. 3(a), exhibits an inhomogeneous morphology with some columnar elements. In Fig. 3(b), the morphology of sample V_1 appears significantly more compact. Samples V_2 and V_3 , presented in Figs. 3(c) and 3(d), respectively, display a very compact and homogeneous morphology. It is noteworthy that all the coatings exhibit a cauliflower surface morphology, where protruding features agglomerate to form larger structures. These structures are

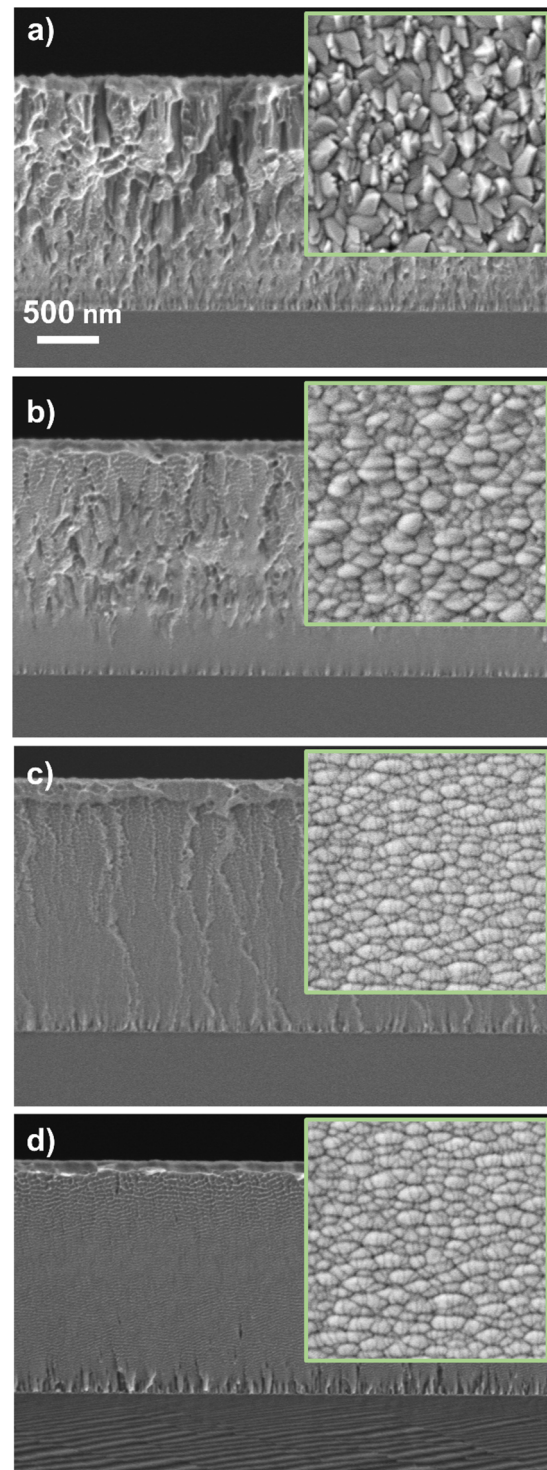


FIG. 3. Cross-sectional and surface morphology (insets) of the TiZrNb(V) coatings. (a) V_0 , (b) V_1 , (c) V_2 , and (d) V_3 . Scale bar is the same for all images including insets.

associated with unstable growth under surface diffusion-limited conditions.⁵³

C. Atomic force microscopy

The surface roughness of the as-deposited samples was determined at room temperature by AFM. Standard analysis provides two main values, Ra and Rq. Ra or “roughness average” stands for the mean roughness and is calculated as the arithmetic average of the absolute values of the roughness profile ordinates. It gives a good general description of the height variations in the surface. Rq is the root mean square (RMS) roughness; therefore, the RMS average of the roughness profile ordinates.

Uniform nanostructures were clearly observed, and the heights of these undulating nanostructures were less than 7 nm. These experimental images verified the fine nanostructures on the surface of the TiZrNbV coatings, and the surface was very smooth as a whole, with a surface roughness, Ra, of less than 7 nm. The texture (clearer in V₁, V₂, and V₃) in the coating is due to the polishing process in the substrate previous to the deposition.

The surface roughness of the crystalline coatings, V₀ and V₁, was very similar, 6.8 ± 0.3 and 6.6 ± 0.2 nm, respectively. For V₂ and V₃ coatings, the Ra decreases to 4.7 ± 0.2 nm, respectively, probably owing to the refining of the surface structural features and amorphization. So, it appears that in this system thin films with amorphous structure possess lower Ra and Rq roughness as compared to their crystalline counterparts.

Note that the substrate plays a role in the morphology of the film and in its fine details in terms of microstructure and more. It is beyond the scope of the present paper to explore this issue in depth, but it is an important topic for future study (Fig. 4).

D. Mechanical and adhesion properties of as-deposited coatings

The mechanical properties of our TiZrNbV coatings were evaluated using nanoindentation. Specifically, we have evaluated the hardness and Young’s modulus. In the process of forming a solid solution, the lattice distortion arises due to the atomic size effect. This phenomenon elucidates the impact of the atomic size effect on the alloy’s hardness.⁵⁵

The hardness values of as-deposited V₀, V₁, V₂, and V₃ are 12.0, 13.8, 12.6, and 12.9 GPa, respectively. Ternary V₀ coating reveals a slightly lower hardness value. Including a greater number of constituent elements does not ensure improved structural properties. A higher cohesive energy among atoms in a lattice demands increased shear stresses to rupture metallic bonds, thereby enhancing stiffness. An alloy with fewer elements may inherently possess a higher cohesive energy than one with a greater number of elements in the same series, consequently surpassing the higher-entropy alloy in terms of structural properties.⁵⁶

Figure 5 shows the marks generated by the scratch tester to assess the adhesion of coatings to the substrate. By observing Fig. 5(a), it is evident that the adhesion of the reference coating (V₀), which does not contain V, is lower than the others. The first cohesive failure occurs at 0.15 mm, which corresponds to a critical load (Lc1) of 3.35 N, while the first adhesive failure appears at 4.50 mm and corresponds to a critical load (Lc2) of 42.5 N. However, there is no total failure of the coating (Lc3). There are also visible spalling effects (chipping) along the sample, indicators of poor adhesion.

In sample V₁, Fig. 5(b), only a first cohesive failure is visible at 2.19 mm, which corresponds to a critical force (Lc1) of 21.7 N. In sample V₂, there are no visible flaws, as well as in V₃, represented in Figs. 5(c) and 5(d). It is evident that V additions improve the adhesion of the coatings to the substrate.

E. Oxidation resistance

Figure 6(a) shows the results of the dynamic oxidation tests carried out on the coatings. The reference sample V₀ begins its oxidation at a temperature of around 380 °C, slightly higher than the temperature at which the rest of the coatings are starting their oxidation. This indicates that the addition of V lowers the onset point of oxidation (to values around 300 °C). Furthermore, it is possible to observe that the oxidation curves of the coatings with V are deviated for lower temperature values than the reference sample V₀, indicating that they are less resistant to oxidation than the reference V₀ coating. In all the dynamic oxidation graphs, a horizontal plateau is visible. This threshold indicates that the coatings were fully oxidized. It should also be noted that the total mass gain is different for all coatings. The higher the concentration of V in the

20 January 2025 18:57:12

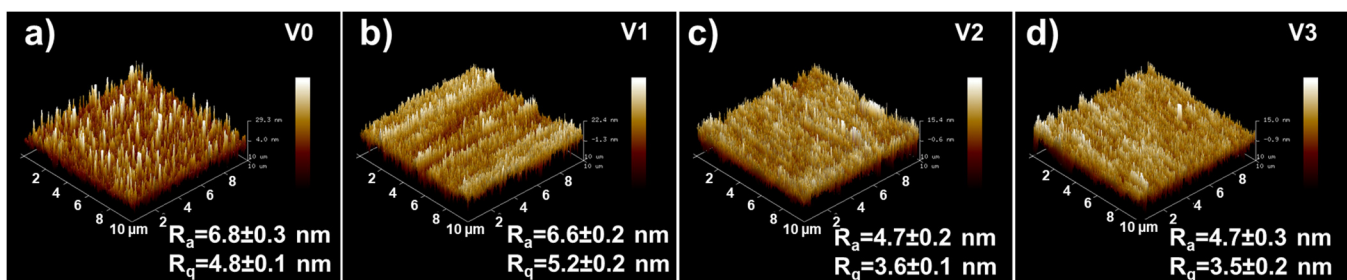


FIG. 4. 3D AFM images of a surface topography of the TiZrNb(V) coatings. From left to right, (a) V₀, (b) V₁, (c) V₂, and (d) V₃ as labeled. Ra and Rq values are provided in the bottom right corner.

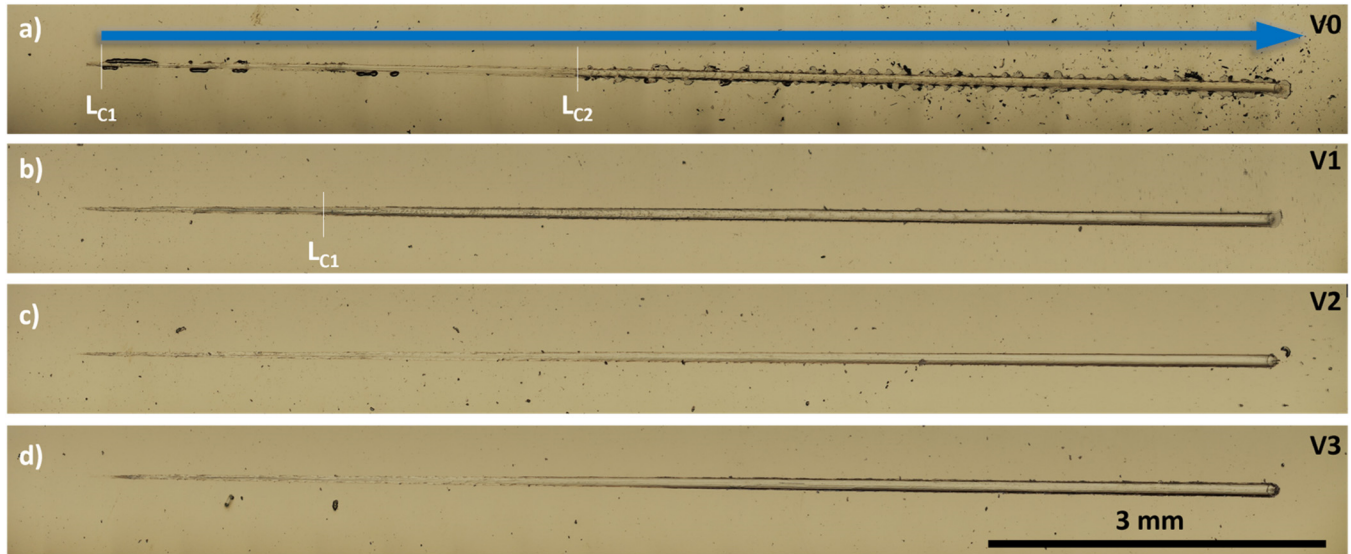


FIG. 5. Optical images of the scratches after adhesion tests of the TiZrNb(V) coatings with access critical load values: (a) V₀, (b) V₁, (c) V₂, and (d) V₃.

coating, the greater the mass gain acquired is. This behavior is due to the combined effect of (i) an increase in the thickness of the coatings with an increase in V (more material to oxidize which implies more mass gain) and (ii) mass gain due to the formation of vanadium oxide—V₂O₅. The ratio between V and O in the V₂O₅ phase is greater than the ratio of the other oxides formed (e.g., TiO₂) leading to a greater mass gain the higher the concentration of V. Note that the coatings V₂ and V₃ have the same thickness and, therefore, the greater mass gain of the last coating can be explained by the formation of a greater amount of vanadium oxide. It is noteworthy that, although V-doped TiZrNb coatings exhibited

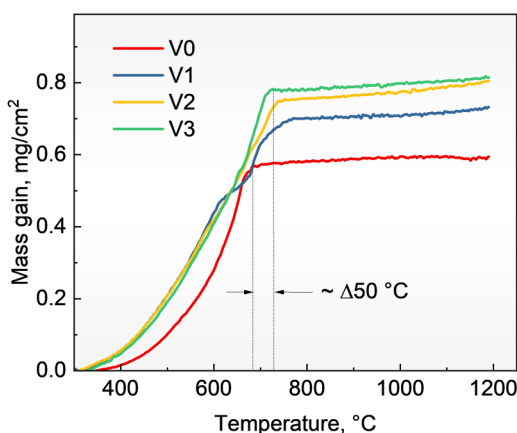


FIG. 6. TG curves of the TiZrNb(V) coatings tests in the linear dynamic heating mode.

a higher mass gain, they were fully oxidized at a higher temperature (730 °C) compared to the TiZrNb coatings, which fully oxidized at 680 °C.

Figure 7(a) shows the results of the isothermal oxidation tests carried out on the coatings. As expected, according to the dynamic oxidation curves, the V₀ coating has the best resistance to oxidation, showing a mass gain of 0.11 mg/cm². The introduction of V in the coating leads to an increase in mass gain. This progressively increases with increasing V concentration up to 21.5 at. % and then decreases slightly for the V₃ coating. Therefore, although in the dynamic tests, the curves of the V-rich coatings are very similar and suggest that they have similar oxidation resistance, the isothermal curves clarify that there is an increase in mass gain due to oxidation with increasing V concentration, with the exception of the V₃ coating. This decrease in the oxidation resistance of coatings with the addition of V has already been studied for other coating systems, and according to the literature, it results from the rapid diffusion of V to the surface, which leaves behind a porous layer, preventing the formation of continuous protective layers.⁵⁴ In fact, although a higher concentration of V enables greater diffusion of this element to the surface, the degree of compactness of the coating can delay this diffusion and could explain this behavior. Also, the higher compactness means less “porous” coating, which also halts the entrance of oxygen into the coating to help with the formation of the vanadium oxide (even if only in the beginning of the oxidation process). By having higher “porosity,” there is also higher surface area in contact with the atmosphere.

Figures 7(b)–7(e) show the cross section of the coatings after oxidation and the respective elementary distribution lines of the main chemical elements of the coatings. As can be seen in Fig. 7(b), the reference sample V₀ has a very small, oxidized zone (see the intensity of the oxygen signal), which corroborates its low

20 January 2025 18:57:12

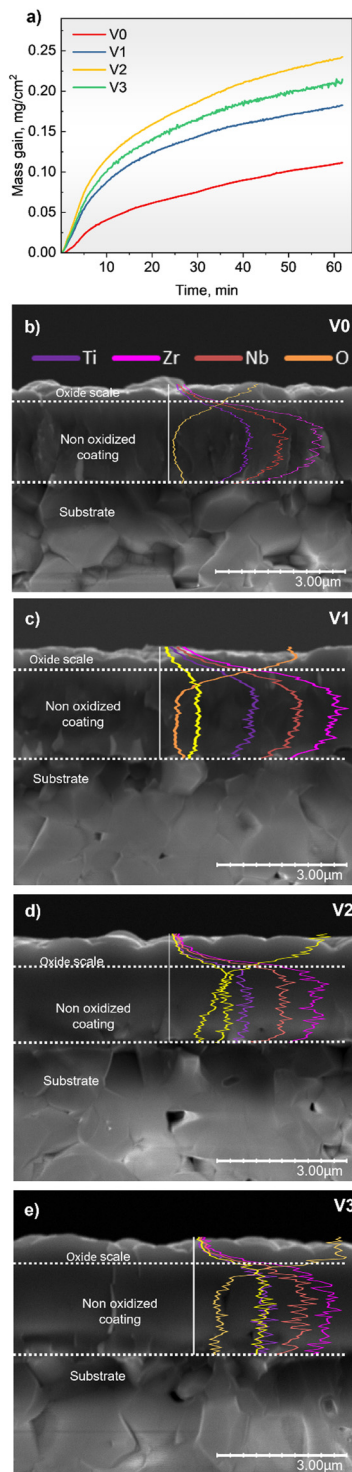


FIG. 7. (a) Isothermal TGA mass gain curves for TiZrNb(V) coatings. (b)–(e) Cross-sectional images of the coatings oxidized at 400 °C for 1 h with chemical profiles acquired from the cross section are available: (b) V₀, (c) V₁, (d) V₂, and (e) V₃.

mass gain due to oxidation shown in Fig. 7(a). The addition of V leads to the formation of a thicker oxide layer, as seen in Figs. 7(d) and 7(e). The low resolution of the SEM equipment might render the pore morphology nondiscernible in the cross-sectional images.

Finally, it is worth mentioning that oxidation tests of various HEAs revealed a complex nature of oxides. In our case, the passivation film can be composed of TiNb₂O₇, VO₂, V₂O₃, TiO₂, and Nb₂Zr₆O₁₇ oxides.^{57,58} For V-doped refractory alloys, the oxide mixture did not improve high-temperature oxidation resistance, as oxidation primarily occurred through internal processes. The specific sequence of reactions for the Ti-Zr-Nb-(V) oxide mixture remains unclear. On the other hand, the formation of V₂O₃ and VO₂ oxides inhibits molten salt corrosion and enhances material performance during prolonged contact with biomimetic media.^{59,60}

F. Structure and mechanical properties of the coatings after annealing

To analyze the thermal stability of the coatings, they underwent an annealing treatment at a temperature of 400 °C for 200 protective atmosphere of hydrogenated argon (Ar + H₂–5 vol. %) at 0.1 Pa. Subsequently, the structure, hardness, and Young's modulus were reassessed and compared with the properties of the samples in the as-deposited state.

As depicted in Figs. 8(a), and 8(e), the (110) peak after the annealing is observed at a slightly higher 2θ value than before. This phenomenon can be associated with the release of internal stress and some minor rearrangements within a structure. Notably, the bcc structure of V₀ and V₁ samples remains stable for annealing up to 400 °C. GIXRD configuration does not allow us to estimate the size of the grains correctly, so FWHM values can be used only for qualitative analysis. For V₀ coating before and after annealing, FWHM values were of 0.75°; in the case of the V₁ sample, it insignificantly decreased from 0.85° to 0.79°. Shape and signal-to-noise ratio of V₂ and V₃ GIXRD patterns after annealing do not allow to fit the peak; meanwhile, one can see no signs of crystallization [Fig. 8(c)]. Figure 8(b) shows the hardness and Young's modulus values of the coatings before and after annealing. It is possible to observe that, after heat treatment, the hardness value increases for all coatings. Displacement of diffraction peaks toward higher angles [Fig. 8(e)] typically represents a loss of residual compressive stresses and a consequent decrease in mechanical properties;⁶¹ this shift was observed after annealing in case of V₀ and V₁ coatings, but mechanical properties increased in our study.

Further, the mechanical properties of the system may be dependent on a variety of factors, like possible local chemical inhomogeneities (as in other TiZrNb-based refractory HEAs, Ref. 62), on precipitates of unwanted phases,⁶³ nanoscale details such as atomic packing density,⁶⁴ and on oxygen content.^{53,54} Therefore, the exact mechanisms that favor the adhesion properties depending on the V content are beyond the scope of the present work.

As screening parameters, both H/E and H³/E² have considerable merit and have demonstrated many successes; for hard coatings, these proxies are used to relate resistance to crack initiation and tribological performance. For hard PVD coatings, higher H/E promoted lower wear.^{65,66}

20 January 2025 18:57:12

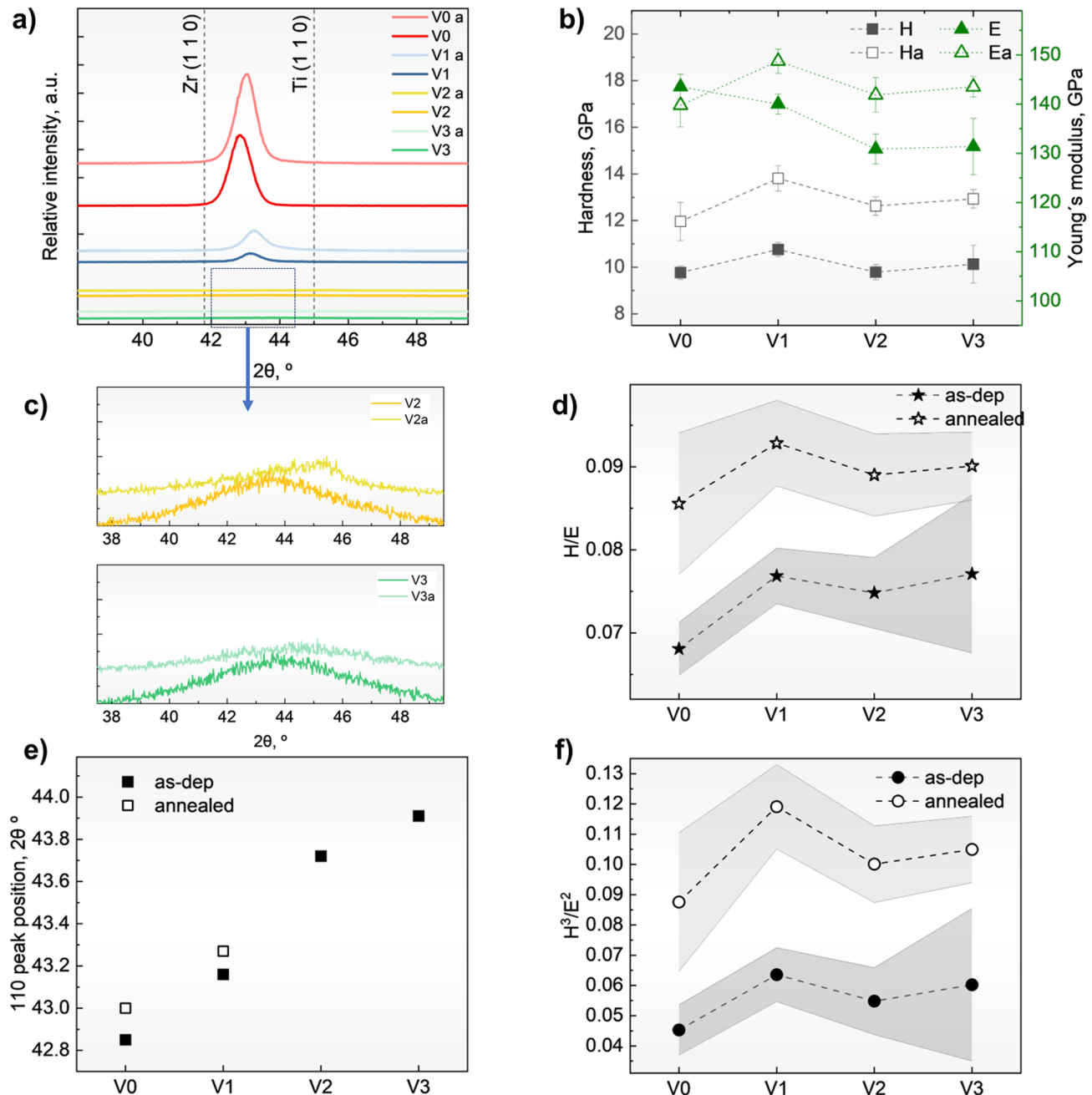


FIG. 8. (a) GIXRD patterns of the coatings before and after annealing. (b) Hardness (left y-axis), and Young's modulus (right y-axis) measured in as-deposited samples (solid symbols) and after being annealed at 400 °C for 2 h (open symbols). (c) Zoom of the XRD patterns of V₂ and V₃ as-deposited and annealed. (d) H/E ratio values, (e) 2θ position of the 110 peak, and (f) H^3/E^2 ratio values.

Other results suggest that optimizing the H/E ratio across the coating and substrate could enhance the adhesion strength of the coating by redistributing the surface contact stresses.⁶⁷ Interestingly, our results show that V alone does not affect

hardness. However, adding V to Ti-Zr-Nb refractory alloy coatings increases both the H/E and H^3/E^2 values. Heat treatment of as-deposited coatings caused a noticeable increase in the values of H/E and H^3/E^2 proxies. These results suggest that annealing of the

Ti-Zr-Nb-(V) coatings can be used as a very effective tool for mechanical properties tuning. In the case of purely crystalline HEAs, lattice-distortion effect can tailor mechanical properties.⁶⁸

The study of the mechanical properties of nanocrystalline/glassy HEAs demonstrated an extrinsic shift from an inverse to a regular Hall–Petch relationship during nanocrystallization and grain coarsening caused by annealing. Furthermore, grain boundary relaxation processes were identified, which led to increased hardness without notable grain growth after annealing at temperatures below 500 °C. In the case of x-ray amorphous materials, the enhancement in mechanical properties might be explained as follows: low temperature annealing (200–400 °C) leads to structural relaxation, as the amorphous domains and interphase regions reorganize to a lower energy state, the second mechanism involves the breakdown of the material’s initial glassy character, which leads to the redistribution of excess free volume from the interphase regions into areas of short-range order.⁶⁹

IV. SUMMARY AND CONCLUSIONS

In the present work, refractory multiprincipal-element alloy coatings in TiZrNb(V) system were deposited by the HiPIMS process. The concentration ratios of Zr/Ti, Nb/Ti, and Nb/Zr were similar when V concentration was increasing from 0 to 28.5 at. %. Morphology, structure, resistance to oxidation, and thermal stability of the coatings and evaluation of V concentration impact on these properties were studied.

The results obtained throughout the work allowed drawing the following conclusions:

- (i) The increase in V content in TiZrNb(V) coatings led to an increase in the degree of compactness of the microstructure, which was also accompanied by transition from bcc crystalline to the x-ray amorphous structure.
- (ii) The hardness of the as-deposited coatings in the TiZrNb(V) system was very similar irrespective of the V concentration. Values in the range of 10–11 GPa were obtained. Young’s modulus values are slightly higher for the V₀ and V₁ coatings, both exhibiting a crystalline structure (140 GPa). However, as the V content increases, leading to the transition to an amorphous structure, there is a subsequent decrease in Young’s modulus (130 GPa).
- (iii) Annealing under a protective atmosphere enhanced the mechanical properties of the TiZrNb(V) coatings, regardless of composition. It was demonstrated that values for hardness (H), elastic modulus (E), H/E ratio, and H³/E² ratio can be effectively adjusted by heat treatment at low temperatures, which prevents grain growth and nucleation.
- (iv) Scratch tests of TiZrNb(V) coatings deposited on steel substrates were carried out. Critical load, Lc1, increases with the increase in V content in the alloy coatings demonstrating the improved adhesion to the substrate. Failure mechanism for V₀ and V-doped V₁, V₂, and V₃ was different: spalling and chipping along the sample, proved poor adhesion properties of the V₀ coating. In samples with V addition, there were no visible flaws, making evident that V improves the adhesion of the coatings to the substrate.

- (v) Dynamic and isothermal oxidation tests demonstrated that TiZrNb coatings exhibited slower and lower overall mass gain compared to V-doped TiZrNb coatings. The addition of vanadium in the TiZrNb system resulted in the formation of a thicker oxide scale after isothermal oxidation at 400 °C. However, during dynamic oxidation tests, TiZrNbV coatings (V₁, V₂, and V₃) were fully oxidized at around 730 °C, whereas TiZrNb V₀ coatings reached complete oxidation at 680 °C.

ACKNOWLEDGMENTS

This project has been possible, thanks to the Bangor University Innovation and Impact Awards 2022. A. Fraile is funded through the Sêr Cymru II 80761-BU-103 project by Welsh European Funding Office (WEFO) under the European Development Fund (ERDF). This research was also sponsored by FEDER funds through the program COMPETE—Programa Operacional Factores de Competitividade—and by national funds through FCT—Fundação para a Ciência e a Tecnologia, under the projects: CEMMPRE—Ref. “UIDB/00285/2020” and ARISE—Ref. “LA/P/0112/2020.”

AUTHOR DECLARATIONS

Conflict of Interest

The authors have no conflicts to disclose.

Author Contributions

A. Fraile: Funding acquisition (lead); Investigation (equal); Project administration (lead); Writing – original draft (equal). **D. Cavaleiro:** Data curation (equal); Formal analysis (equal). **A. Bondarev:** Data curation (equal); Formal analysis (equal); Investigation (equal); Writing – original draft (equal). **S. C. Middleburgh:** Formal analysis (equal); Investigation (equal); Writing – original draft (equal). **W. E. Lee:** Formal analysis (equal); Investigation (equal); Writing – original draft (equal). **F. Fernandes:** Data curation (equal); Formal analysis (equal); Investigation (equal); Writing – original draft (equal).

DATA AVAILABILITY

The data that support the findings of this study are available from the corresponding author upon reasonable request.

REFERENCES

- ¹G. S. Was, *J. Nucl. Mater.* **367–370**, 11 (2007).
- ²S. J. Zinkle and J. T. Busby, *Mater. Today* **12**, 12 (2009).
- ³I. Charit and K. L. Murty, *J. Mater.* **62**, 67 (2010).
- ⁴T. Muroga, M. Gasparotto, and S. J. Zinkle, *Fusion Eng. Des.* **61–62**, 13 (2002).
- ⁵A.-A. F. Tavassoli, *J. Nucl. Mater.* **302**, 73 (2002).
- ⁶A. Fraile, Santiago Cuesta-López, Alfredo Caro, Daniel Schwen, and J. Manuel Perlado, *J. Nucl. Mater.* **448**, 103 (2014).
- ⁷A. Fraile and T. Polcar, *Nucl. Fusion* **60**, 046018 (2020).
- ⁸R. Alba, R. Iglesias, and M. A. Cerdeira, *Materials* **15**, 6591 (2022).
- ⁹A. Fraile, P. Dwivedi, G. Bonny, and T. Polcar, *Nucl. Fusion* **62**, 026034 (2022).
- ¹⁰J. T. Busby and K. J. Leonard, *J. Mater.* **59**, 20 (2007).

20 January 2025 18:57:12

- ¹¹S. E. Prameela, Tresa M. Pollock, Dierk Raabe, Marc André Meyers, Assel Aitkaliyeva, Kerri-Lee Chintersingh, Zachary C. Cordero, and Lori Graham-Brady, *Nat. Rev. Mater.* **8**, 81 (2023).
- ¹²H. Yavas, Alberto Fraile, Teodor Huminiuc, Huseyin Sener Sen, Emilio Frutos, and Tomas Polcar, *ACS Appl. Mater. Interfaces* **11**, 46296 (2019).
- ¹³S. Zhang, D. Sun, Y. Fu, and H. Du, *Surf. Coat. Technol.* **167**, 113 (2003).
- ¹⁴M. F. Montemor, *Surf. Coat. Technol.* **258**, 17 (2014).
- ¹⁵P. Moriarty, *Rep. Prog. Phys.* **64**, 297 (2001).
- ¹⁶R. A. Andrievski, *J. Mater. Sci.* **38**, 1367 (2003).
- ¹⁷D. B. Miracle and O. N. Senkov, *Acta Mater.* **122**, 448 (2017).
- ¹⁸R. Feng, Michael Gao, Chanho Lee, Michael Mathes, Tingting Zuo, Shuying Chen, Jeffrey Hawk, Yong Zhang, and Peter Liaw, *Entropy* **18**, 333 (2016).
- ¹⁹J. A. Wilson, Lee J Evitts, Alberto Fraile, Roy E Wilson, Michael J D Rushton, David T Goddard, William E Lee, and Simon C Middleburgh, *J. Phys.* **4**, 034002 (2022).
- ²⁰K. A. Kuptsov *et al.*, *Surf. Coat. Technol.* **453**, 129136 (2023).
- ²¹E. J. Pickering, Alexander W. Carruthers, Paul J. Barron, Simon C. Middleburgh, David E. J. Armstrong, and Amy S. Gandy, *Entropy* **23**, 98 (2021).
- ²²D. J. M. King, S. T. Y. Cheung, S. A. Humphry-Baker, C. Parkin, A. Couet, M. B. Cortie, G. R. Lumpkin, S. C. Middleburgh, and A. J. Knowles, *Acta Mater.* **166**, 435 (2019).
- ²³A. Kareer, J. C. Waite, B. Li, A. Couet, D. E. J. Armstrong, and A. J. Wilkinson, *J. Nucl. Mater.* **526**, 151744 (2019).
- ²⁴J. Li, Yongxian Huang, Xiangchen Meng, and Yuming Xie, *Adv. Eng. Mater.* **21**, 1900343 (2019).
- ²⁵A. Sharma, *Coatings* **11**, 372 (2021).
- ²⁶A. Meghwal, Aamey Anupam, B. S. Murty, Christopher C. Berndt, Ravi Sankar Kottada, and Andrew Siao Ming Ang, *J. Therm. Spray Technol.* **29**, 857 (2020).
- ²⁷Y. Li, Chunting Wang, Donglin Ma, Xiaokang Zeng, Mao Liu, X. Jiang, and Y. X. Leng, *Surf. Coat. Technol.* **420**, 127325 (2021).
- ²⁸H. Cheng, Zhimin Pan, Yu Fu, Xuefei Wang, Ya Wei, Hong Luo, and Xiaogang Li, *J. Electrochem. Soc.* **168**, 111502 (2021).
- ²⁹K. K. Kadyrzhanov, Artem L. Kozlovskiy, Dmitriy I. Shlimas, Daryn B. Borgekov, Sholpan G. Giniyatova, Vladimir V. Uglov, and Maxim V. Zdorovets, *Metals* **13**, 727 (2023).
- ³⁰A. X. Lin-Vines, J. A. Wilson, A. Fraile, Lee J. Evitts, M. J. D. Rushton, J. O. Astbury, W. E. Lee, and S. C. Middleburgh, *Results Mater.* **15**, 100320 (2022).
- ³¹B. Yin, F. Maresca, and W. A. Curtin, *Acta Mater.* **188**, 486 (2020).
- ³²C. R. Das, M. Rangwala, and A. Ghosh, *Surf. Coat. Technol.* **458**, 129351 (2023).
- ³³W. Tillmann, Nelson Filipe Lopes Dias, Dominic Stangier, Wolfgang Maus-Friedrichs, René Gustus, Carl Arne Thomann, Henning Moldenhauer, and Jörg Debus, *Surf. Coat. Technol.* **375**, 877 (2019).
- ³⁴H. Hajihoseini and J. T. Gudmundsson, *J. Phys. D: Appl. Phys.* **50**, 505302 (2017).
- ³⁵W. F. Cui and C. J. Shao, *Surf. Coat. Technol.* **283**, 101 (2015).
- ³⁶J. Zhang, Hefeng Wang, Shangyu Yang, Xuegang Xing, Xuefeng Shu, and Xiaomin Jin, *Mater. Corros.* **69**, 1703 (2018).
- ³⁷P. F. Ji, B. Li, B. H. Chen, F. Wang, W. Ma, X. Y. Zhang, M. Z. Ma, and R. P. Liu, *Corros. Sci.* **170**, 108696 (2020).
- ³⁸S. Hu, Taojun Li, Zhenqian Su, Shuaiju Meng, Zhi Jia, and Dexue Liu, *Mater. Sci. Eng. B* **270**, 115226 (2021).
- ³⁹J. Mu, Haiyan Wang, Binhao Qin, Yupeng Zhang, Lijia Chen, and Caiyou Zeng, *Surf. Coat. Technol.* **428**, 127866 (2021).
- ⁴⁰C. B. A. Forty and P. J. Karditsas, *J. Nucl. Mater.* **283–287**, 607 (2000).
- ⁴¹Q. Xing, A. C. Feltrin, and F. Akhtar, *Wear* **510–511**, 204497 (2022).
- ⁴²M. Wang, Z. L. Ma, Z. Q. Xu, and X. W. Cheng, *Scr. Mater.* **191**, 131 (2021).
- ⁴³M. El Garah, Driss Soubane, and Frederic Sanchette, *Emerg. Mater.* **7**, 77 (2024).
- ⁴⁴D. J. M. King, S. C. Middleburgh, A. C. Y. Liu, H. A. Tahini, G. R. Lumpkin, and M. B. Cortie, *Acta Mater.* **83**, 269 (2015).
- ⁴⁵M. Marczewski, K. Wiecek, X. Maeder, L. Lapeyre, C. Hain, M. Jurczyk, and T. Nelis, *J. Mater. Sci.* **59**, 9107 (2024).
- ⁴⁶B.-S. Lou, Ren-Zong Lin, Chia-Lin Li, and Jyh-Wei Lee, *Surf. Coat. Technol.* **483**, 130772 (2024).
- ⁴⁷S. Kamrudin Bachani, Chaur-Jeng Wang, Bih-Show Lou, Li-Chun Chang, and Jyh-Wei Lee, *J. Alloys Compd.* **873**, 159605 (2021).
- ⁴⁸F. Fernandes, V. S. Calderon, P. J. Ferreira, A. Cavaleiro, and J. C. Oliveira, *Surf. Coat. Technol.* **397**, 125996 (2020).
- ⁴⁹W. H. Bragg and W. L. Bragg, *Proc. R. Soc. London Ser. A* **88**, 605 (1913).
- ⁵⁰See <https://www.yumpu.com/en/document/view/3911284/periodic-table-of-elements-and-x-ray-energies-msitechnet> for “Periodic table of elements and x-ray energies—Msitech.net” (accessed June 7, 2023).
- ⁵¹S. Guo, Q. Hu, C. Ng, and C. T. Liu, *Intermetallics* **41**, 96 (2013).
- ⁵²A. Liang, Daniel C. Goodelman, Andrea M. Hodge, Diana Farkas, and Paulo S. Branicio, *Acta Mater.* **257**, 119163 (2023).
- ⁵³F. Fernandes, J. Morgiel, T. Polcar, and A. Cavaleiro, *Surf. Coat. Technol.* **275**, 120 (2015).
- ⁵⁴M. Athmani, A. AL-Rjoub, D. Cavaleiro, A. Chala, A. Cavaleiro, and F. Fernandes, *Surf. Coat. Technol.* **405**, 126593 (2021).
- ⁵⁵Y. Jing, Xiufang Cui, Guo Jin, Yuyun Yang, Xin Wen, Yajie Guan, and Dan zhang, *J. Alloys Compd.* **856**, 158128 (2021).
- ⁵⁶A. Roy, Praveen Sreeramagiri, Tomas Babuska, Brandon Krick, Pratik K. Ray, and Ganesh Balasubramanian, *Mater. Charact.* **172**, 110877 (2021).
- ⁵⁷V. Grajewski, H. H. Uchida, and E. Fromm, *Thin Solid Films* **193–194**, 990 (1990).
- ⁵⁸W. Xiong, Amy X.Y. Guo, Shuai Zhan, Chain-Tsuan Liu, and Shan Cecilia Cao, *J. Mater. Sci. Technol.* **142**, 196 (2023).
- ⁵⁹F. Cemin, Leonardo Luis Artico, Vanessa Piroli, José Andrés Yunes, Carlos Alejandro Figueroa, and Fernando Alvarez, *Appl. Surf. Sci.* **596**, 153615 (2022).
- ⁶⁰K. Patel, Maryam Sadeghilaridjani, Mayur Pole, and Sundeep Mukherjee, *Sol. Energy Mater. Sol. Cells* **230**, 111222 (2021).
- ⁶¹X. G. Wang, M. Sun, J. X. Liu, X. Q. Liu, Y. B. Ke, W. B. Jiang, H. Wang, Q. F. Fang, and X. P. Wang, *J. Alloys Compd.* **987**, 174227 (2024).
- ⁶²K. Xun, Bozhao Zhang, Qi Wang, Zhen Zhang, Jun Ding, and En Ma, *J. Mater. Sci. Technol.* **135**, 221 (2023).
- ⁶³Y. Jiang, X. G. Wang, Z. Q. Jiang, M. Chen, M. Sun, and X. F. Zhang, *J. Alloys Compd.* **937**, 168458 (2023).
- ⁶⁴K. W. Park, Jae-il Jang, Masato Wakeda, Yoji Shibusaki, and Jae-Chul Lee, *Scr. Mater.* **57**, 805 (2007).
- ⁶⁵S. J. McMaster, Shahriar Kosarieh, Tomasz W. Liskiewicz, Anne Neville, and Ben D. Beake, *Tribol. Int.* **185**, 108524 (2023).
- ⁶⁶B. D. Beake, *Surf. Coat. Technol.* **442**, 128272 (2022).
- ⁶⁷H.-K. Kim, Joung-Hyun La, Kyu-Sung Kim, and Sang-Yul Lee, *Surf. Coat. Technol.* **284**, 230 (2015).
- ⁶⁸C. Lee *et al.*, *Adv. Mater.* **32**, 2004029 (2020).
- ⁶⁹M. J. R. Haché, Y. Zou, and U. Erb, *Surf. Coat. Technol.* **482**, 130719 (2024).